Chemical Engineering Journal 508 (2025) 161091

Contents lists available at ScienceDirect

Chemical Engineering Journal

journal homepage: www.elsevier.com/locate/cej

Janus NPs@MOFs-based nanosensors for real-time visual monitoring and enhanced therapy of colon cancer

Jukun Yang [a], Mo Ma [a,c], Chen Zhao [a], Yuxuan Chen [a], Jingdan Sun [d], Ying Sun [a], Pinyi Ma [a,*], Shan Jiao [b,*], Daqian Song [a,*]

[a] College of Chemistry, Jilin Province Research Center for Engineering and Technology of Spectral Analytical Instruments, Jilin University, Qianjin Street 2699, Changchun 130012, PR China
[b] Hospital of Stomatology, Jilin University, Qinghua Road 1500, Changchun 130021, PR China
[c] School of Pharmacy, Jilin University, Qianjin Street 2699, Changchun 130012, PR China
[d] Department of Chemistry, University of Washington, Seattle, WA, USA

ARTICLE INFO

Keywords:
Janus nanosensor
Tumor efficacy evaluation
Visual imaging
Tumor combination therapy

ABSTRACT

Colon cancer remains a major cause of cancer-related mortality, which necessitates continuous advancement in treatment efficacy and prognosis evaluation methods. Despite the progress, existing imaging techniques often fail to provide timely, real-time insights in dynamic tumor environments. Thus, achieving precise targeting and effective visualization during treatment remains challenging. In this study, we address these limitations by developing an asymmetric nanosensor based on a core–shell Janus NPs@MOFs centered on gold nanorods (Au NRs) with photothermal capabilities. The nanoparticles were modified with titanium dioxide (TiO_2) to form Janus ATs (J ATs), functionalized with Cy5.5-pep, and coated with folic acid (FA)-doped zeolite imidazole framework-8 (ZIF-8) to allow for targeted cancer cell delivery and confer responsiveness to a weakly acidic environment. This configuration enabled the release of Zn^{2+} under acidic conditions while inducing ion overload and enhancing reactive oxygen species (ROS) production in mitochondria. This approach could effectively promote tumor cell death. Laser irradiation-activated photodynamic therapy (PDT) and photothermal therapy (PTT) synergistically promoted apoptosis via caspase-3 activation and restored fluorescence signal, which led to tumor ablation. Additionally, the nanosensor utilized ion interference therapy (IIT) to disrupt ion homeostasis in tumor cells, which further enhanced therapeutic efficacy. The J ATPZFs (Janus Au NRs-TiO_2-pep@ZIF-8-FA) nanosensor was successfully applied to *in vitro* and *in vivo* imaging, which is demonstrative of its potential for real-time monitoring and as an adjuvant therapeutic tool for colon cancer treatment. This work provides a reference for achieving the goals in the precise, real-time visual monitoring of cancer prognosis.

1. Introduction

Colon cancer is one of the main types of cancer. Although its occurrence has a low percentage, colon cancer is a serious threat to human health due to its high incidence rate and mortality rate [1–5]. With the continuous development of medical technology, common treatment methods such as surgery, chemotherapy, and radiotherapy are constantly being improved and applied in the treatment of this disease [6–9]. For early-stage tumors, the cure rate increases after surgical removal of the primary tumor. With the improvement of science and technology, the supervision of the treatment process and its efficacy have become a concern for medical workers [10–13]. This result is closely related to the patient's prognostic status, and timely and effective feedback on the efficacy is required to improve the treatment plan. Therefore, the visualization and monitoring of the diseased area in real-time remains a challenge that needs to be resolved.

In the field of imaging, the detection of biomarkers using fluorescence nanosensors based on the Förster resonance energy transfer (FRET) effect has attracted considerable attention and been widely used due to the probes' characteristics such as simple operation, powerful imaging ability, and high signal-to-noise ratio [14–16]. The use of FRET detection methods can greatly increase the sensitivity and applicability

* Corresponding authors at: College of Chemistry, Jilin Province Research Center for Engineering and Technology of Spectral Analytical Instruments, Jilin University, Qianjin Street 2699, Changchun, 130012, PR China (P. Ma).
E-mail addresses: mapinyi@jlu.edu.cn (P. Ma), jiaoshan@jlu.edu.cn (S. Jiao), songdq@jlu.edu.cn (D. Song).

https://doi.org/10.1016/j.cej.2025.161091
Received 26 November 2024; Received in revised form 18 February 2025; Accepted 26 February 2025
Available online 27 February 2025

of nanosensors. The effective combination of fluorescence imaging and nanosensors for tumor efficacy evaluation provides a solution for visual real-time monitoring capability. As an important biological target in apoptosis, caspase-3 can be activated during the treatment of tumors [17–19]. Therefore, the use of caspase-3 as the detection target of the nanosensors can play a certain role in the evaluation of the therapy. Additionally, because caspase-3 can recognize the amino acid sequence of special fragments, it provides good selectivity [20–22].

The local surface plasmon resonance (LSPR) effect is commonly observed in some precious metal nanoparticles, which can provide the nanoparticles with a thermal effect after laser irradiation [23–25]. In addition to the use of heat produced after laser irradiation in photothermal therapy (PTT), photodynamic therapy (PDT) is another common light therapy in tumor treatment used to achieve the ablation of tumors [26–28]. At the same time, the effective implementation of PTT and PDT is inseparable from the production of heat and reactive oxygen species (ROS) by photosensitizer and photosensitizer, respectively [29–32]. By optimizing the synthesis process to integrate the two media, the assembly of materials and double promotion can be achieved simultaneously. Among all, gold nanorods are widely used as a photothermal sensitive agent due to their excellent properties [33–35]. By improving the synthesis method, a photosensitizer, titanium dioxide (TiO_2), can be effectively modified on one end of gold nanorods (Au NRs) to form asymmetric nanoparticles J ATs (Janus Au NRs-TiO_2) to combine the advantages of the materials. In addition to the above treatment methods, the abnormal accumulation of ions can lead to changes in the physiological environment in the cells by disrupting ion homeostasis and inducing cell damage through a process called “ion interference therapy (IIT)” [36–38]. The overload of Zn^{2+} can greatly promote the production of ROS in mitochondria and induce cell death [39,40]. This principle can work synergistically with PDT to promote ROS production. In this work, we coated the nanosensor with MOFs material ZIF-8 and used it as the nanosensor shell. Then, a Zn^{2+} carrier was introduced to allow for the simultaneous response to the tumor microenvironment (TME) and to increase the content of Zn^{2+} in tumor cells, which in turn increased the production of ROS, leading to adjuvant combination therapy.

Here, to synchronize the response to the effects of combination therapy, J ATs were first constructed by assembling Au NRs and TiO_2 into the nanosensor. Then, the probe was modified with Cy5.5-modified polypeptide chain, which allows for a specific response to caspase-3, to form Janus Au NRs-TiO_2 NPs-pep (J ATPs). To enhance the tumor-targeting ability of the nanosensor, we modified the folic acid (FA)-doped ZIF-8 outer shell of the nanosensor through self-assembly to generate J ATPZFs (Janus Au NRs-TiO_2-pep@ZIF-8-FA) fabricated based on the core–shell structure of Janus NPs@MOFs [41,42]. J ATPZFs could be injected to allow for real-time visual feedback on the effects of IIT on tumors *in vivo* and simultaneous treatment.

2. Experimental section

2.1. Synthesis of J ATs

Solution A: 400 μL of concentrated Au NRs was added to 100 μL of 0.2 M CTAB solution. Then, 20 mL of anaerobic water was added to the mixture. Solution B: 100 μL of $TiCl_3$ solution was first mixed with 2 mL of anaerobic water before the addition of 350 μL of 1.0 M $NaHCO_3$ solution, which caused the solution color to gradually turn dark blue. Next, 5 mL of solution A was mixed with solution B, and the mixture was gently stirred for 30 min. The product was centrifuged and washed with ethanol. The obtained J ATs were dispersed in ultra-pure water and stored at 4°C.

2.2. Synthesis of J ATPs

The above product (5 mL) was dispersed in 5 mL of water before being mixed with 200 μL of 1 mM mPEG-SH. The mixture was then stirred overnight. The product was collected by centrifugation and dispersed into 5 mL of water. After the addition of 30 μL of 2 mg/mL Cy5.5-pep, the mixture was stirred for 24 h in darkness. The resultant products were collected by centrifugation and washed with water.

2.3. Synthesis of J ATPZFs

Firstly, 10 μL of 0.2 M CTAB solution was mixed vigorously with 1 mL of 1.32 M 2-MIM. Then, 1 mL of 24 mM $Zn(NO_3)_2$ solution was added to the mixture, followed by 1 mL of J ATPs and 1 mL of 1 mg/mL FA. After stirring for 5 min, the mixture was left to stand for 5 h and then washed with methanol to obtain the final products.

2.4. In vitro ·OH detection

First, 600 μL of 100 μg/mL J ATs was mixed with H_2O_2 (1000 μM), and 5 μL of 1 mg/mL MB was then added. After that, the mixture was continuously irradiated with an 808 nm laser (1 W/cm^2). The reaction was carried out for 0, 5, 10, 15, 20, and 30 min. After centrifugation, the UV absorption spectra of the supernatant were recorded. A reaction time of 30 min was selected for subsequent experiments.

The experiment was repeated using H_2O_2 at concentrations of 0, 100, 200, 500, and 1000 μM to verify the effect of H_2O_2 concentration on ROS generation.

2.5. In vitro caspase-3 detection

First, 300 μL of 100 μg/mL J ATPs was mixed with 200 ng/mL caspase-3 and then shaken on an oscillator at 37 °C. The fluorescence intensity of the reaction was measured after 0, 5, 10, 15, 30, 60, and 90 min. The reaction time of 60 min was selected as the optimal reaction time.

J ATPs were diluted with 300 μL of buffer (100 μg/mL) and then incubated with caspase-3 at different concentrations (0, 0.5, 15, 10, 25, 50, 100, or 200 ng/mL). The fluorescence signal of the reaction was measured thereafter.

Verification experiments were also conducted at different times or temperatures to assess the nanosensor’s stability.

A variety of enzymes or molecules were used as disruptors to replace caspase-3 to determine the selectivity of the nanosensor. At the same time, during the incubation of the nanosensor with caspase-3, Z-DEVD-FMK (the inhibitor of caspase-3) was added to inhibit the enzyme before the measurement of the fluorescence signal.

2.6. Detection of cellular ROS production

To further validate the increase in intracellular ROS production, DCFH-DA was used as a fluorescent nanosensor to monitor the intracellular •OH generation. SW620 cells were treated with different conditions described above. After various treatments, the cells were incubated with PBS and DCFH-DA (10 μM) for 30 min before being stained with 1 mM DAPI and stored at 37 °C for 5 min in darkness. Finally, the cells were rinsed with PBS and then subjected to imaging.

2.7. Cell imaging applications

First, a time optimization experiment was carried out to determine the incubation time for fluorescence imaging. The cells were incubated with J ATPZFs (100 μg/mL) and then subjected to imaging after 6, 12, 24, and 36 h. The incubation time of 24 h was in subsequent reactions.

To confirm the performance of the nanosensor, the cells were subjected todifferent treatment conditions: J ATPs, J ATPs + 808 nm laser, J ATPZFs, J ATPZFs + 808 nm laser, and J ATPZFs + 808 nm laser + Z-DEVD-FMK. Fluorescence imaging was performed after 24 h.

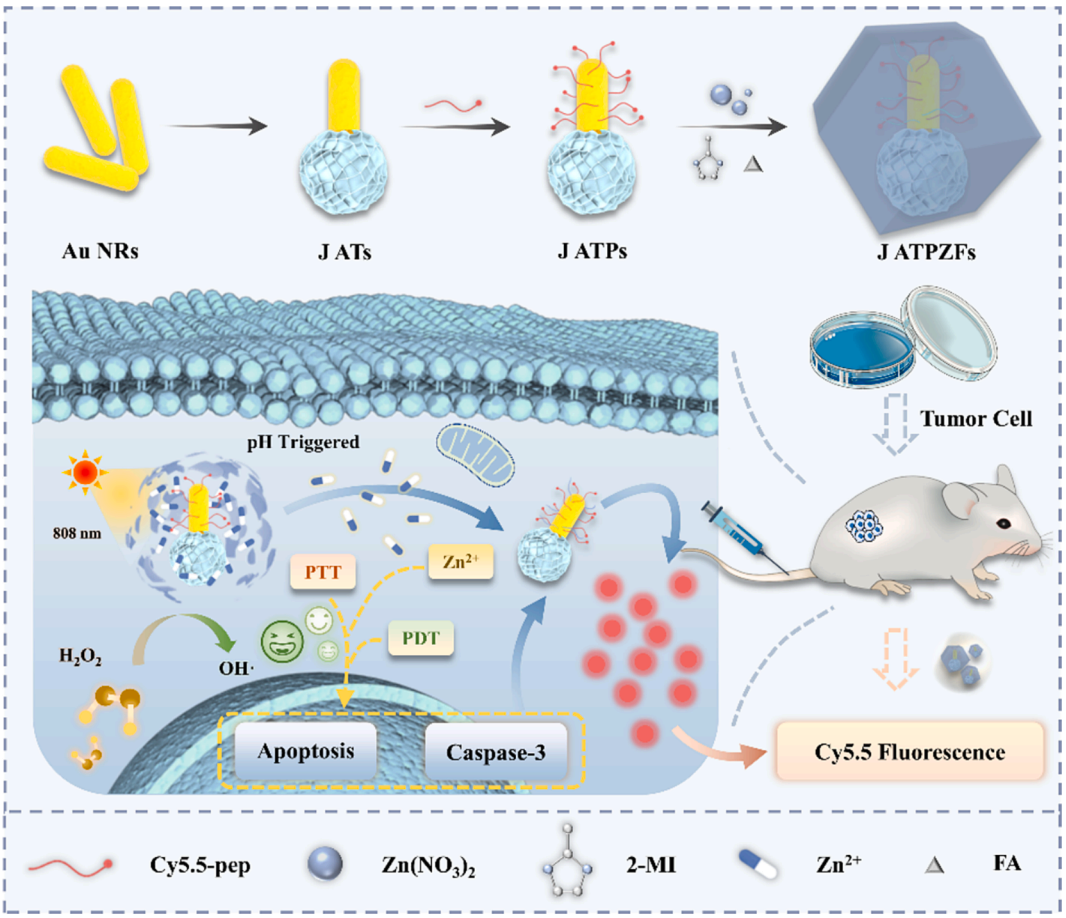

Scheme 1. Schematic illustration of J ATPZFs synthesis process and application.

2.8. In vivo applications

To assess biotoxicity, we injected nanosensors into the tail vein of healthy mice, and stained the heart, liver, spleen, lungs, and kidneys with hematoxylin and eosin (HE) and performed routine blood biochemical analysis 30 days later.

Firstly, the experiments were designed to verify the feasibility of *in vivo* imaging. J ATPs and J ATPZFs (1 mg/mL, 50 μL) were injected *in situ* at the tumor of mice, 808 nm laser irradiation (power: 1 W/cm^2, time: 5 min) was conducted, and the temperature changes were monitored in real-time. At different times after injection, mice were anesthetized with isoflurane before being subjected to imaging.

Next, to confirm the tumor-targeting ability, J ATPs and J ATPZFs (1 mg/mL, 100 μL) was injected into the mouse through the tail vein. The mouse was imaged at 6, 12, and 24 h after injection.

To further evaluate the therapeutic effect of the nanosensors, different experimental groups were set up and compared: PBS, J ATPs, J ATPZFs, and J ATPZFs + 808 nm laser. The weight and tumor volume of the mice were recorded every other day. The tumor volume was calculated by the following formula: V (tumor volume) = [tumor length × tumor width^2]/2.

3. Results and discussion

3.1. Preparation and characterization of nanosensors

The design and synthesis procedure of the nanosensor is shown in Scheme 1. Au NRs were first synthesized and characterized by TEM. The nanoparticles showed an rod-like appearance with a uniform size and excellent dispersion. The crystal lattice of gold could be clearly seen under the High Resolution Transmission Electron Microscope (HRTEM, Fig. 1A). CTAB-modified Au NRs synthesized by the seed growth method had a length-to-diameter ratio of about 62.78 × 15.81 nm (Fig. S1), and the solution was brown (Fig. S2). Then, Janus Au NRs-TiO_2 (J ATs) was synthesized by wet chemistry. Assisted by CTAB, TiO_2 was selectively deposited on Au NRs in an anisotropic manner, and the solution had a purple color. TEM (Fig. 1B), elemental analysis (Fig. S3) and X-ray electron spectroscopy (XPS) (Figs. S4 & S5) were able to confirm the successful synthesis of TiO_2 and the deposition on the top of the gold nanorods. Next, the Cy5.5-peptide, which could be specifically recognized by caspase-3, was modified on J ATs to form the nanosensor J ATPs. To imbue the nanosensor with a Zn^{2+} carrier to enhance ROS production and tumor targeting ability, folic acid (FA)-doped ZIF-8 was modified through self-assembly on the outside of the nanosensor. This modification led to the generation of J ATPZFs based on Janus NPs@MOFs.

UV–Vis absorption spectra of each product were characterized, and the results are shown in Figs. 1D and S8A. The results showed that the near-infrared absorption peak of Au NRs was redshifted after modifications: from 792 nm to 840 nm after TiO_2 modification and from 861 nm to 888 nm after ZIF-8 coating. These processes were confirmed by changes in the zeta potential (Figs. 1E and S8C). The CTAB-modified Au NRs were positively charged, and the potential was changed to −12.3 mV after TiO_2 modification. Then, the peptide was modified to form J ATPs causing the negative charge on the nanosensors to increase (−19.6 mV). After the final coating with doped ZIF-8, the zeta potential also changed. In addition, the XPS of each product was found to correspond to the modification process (Figs. S6 and S7) [43].

The nanostructure of J ATPZFs could effectively maintain the crystalline phase of Au NRs and ZIF-8, which also demonstrates the

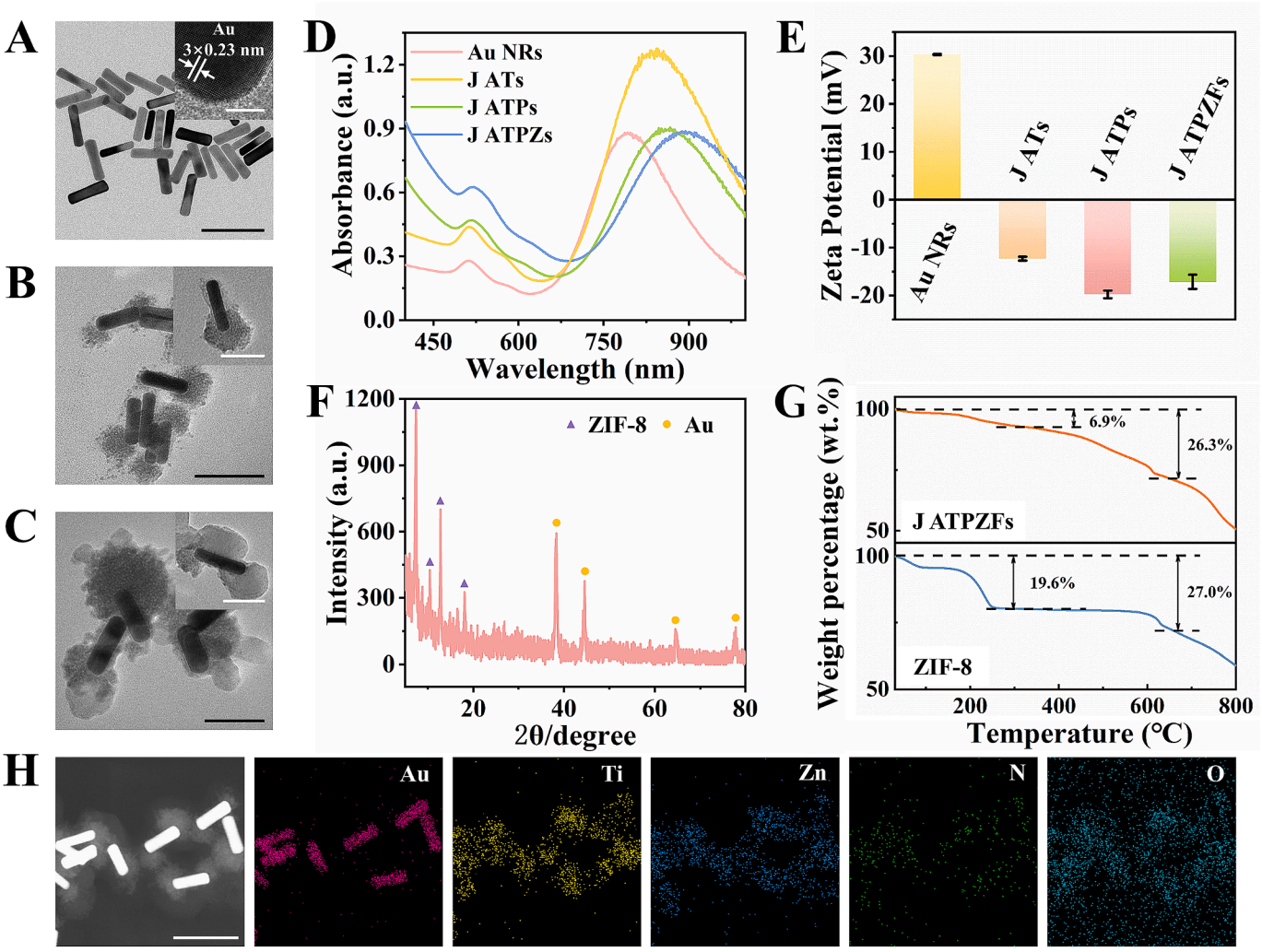

Fig. 1. TEM images of (A) Au NRs (scale bar: 100 nm, scale bar of the inset: 5 nm), (B) J ATs (scale: 100 nm, scale bar of the inset: 60 nm), and (C) J ATPZFs (scale bar: 60 nm). (D) UV–visible absorption spectra of Au NRs, J ATs, J ATPs, and J ATPZFs. (E) Zeta potentials of Au NRs, J ATs, J ATPs and J ATPZFs. (F) XRD images of nanosensor J ATPZFs and the characteristic peak of the control material. (G) Thermogravimetric (TG) curves of J ATPZFs and ZIF-8. (H) TEM mapping of each element of J ATPZFs (scale bar: 100 nm).

coexistence of the two structures (Figs. 1F and S9). Meanwhile, it showed an amorphous state, according to the HRTEM and XRD results (Figs. S9 and S10), without exhibiting obvious diffraction peaks of TiO_2 crystalline, which is consistent with the literature [44]. The TEM-mapping results (Fig. 1H) revealed the elemental distribution of the nanosensor J ATPZFs. The results showed that Ti was mainly distributed at the rod end of Au NRs, and Zn (the characteristic element of ZIF-8) had a slightly wider distribution compared to Ti and Au. This observation is consistent with the arguments described above and proves the effective combination of the components. In addition, the FTIR spectra (Fig. S11) showed the characteristic peaks at 2921 and 2852 cm^{-1}, corresponding to the stretching vibrations of methylene and methyl groups in Au NRs, a strong absorption peak at 500–700 cm^{-1} of TiO_2, and peaks at 1579 (O-H), 1145, and 758 cm^{-1} (imidazolium bending) of ZIF-8 [45]. The peaks confirm the presence of these components. Comparison of the TG curves of the composite nanosensors with those of ZIF-8 revealed that J ATPZFs were thermally stable at 400 °C, similarly to ZIF-8 (Fig. 1G).

3.2. ROS generation capability of nanosensors

The ROS-generating ability of J ATs under laser irradiation is shown in Fig. 2A. According to the reported literature, there is electron transfer from Au NRs to TiO_2 structure under laser irradiation, which can promote ROS production[46,47]. Because methylene blue (MB) can be gradually degraded in the presence of ·OH, MB was chosen as the nanosensor to detect the capability of J ATs in promoting ·OH generation. The MB degradation was verified under different conditions at a fixed reaction time of 30 min. The results demonstrated that the external laser could substantially enhance the ROS production capacity (Fig. 2B). And both the absence of H_2O_2 and J ATs affect the production of ROS. Based on this finding, the relationship between ROS production and laser irradiation time was explored under a constant MB concentration. As shown in Fig. 2C, with increasing laser irradiation time, the MB degradation increased, and the intensity of the corresponding UV–Vis absorption peak became weaker. Similarly, increasing the concentration of raw material H_2O_2 also increased the ROS generation ability (Fig. 2D).

3.3. Photothermal properties of nanosensors

Au NRs are common nanomaterials with excellent photothermal properties. Herein, Au NRs were modified, and all the products were found to have significant Localized Surface Plasmon Resonance (LSPR) absorption at 808 nm (Figs. 1D and S8A). The photothermal properties of the nanosensors, using J ATs as an example, were then validated.

In this experiment, an 808 nm near-infrared laser (1 W cm^{-2}) was

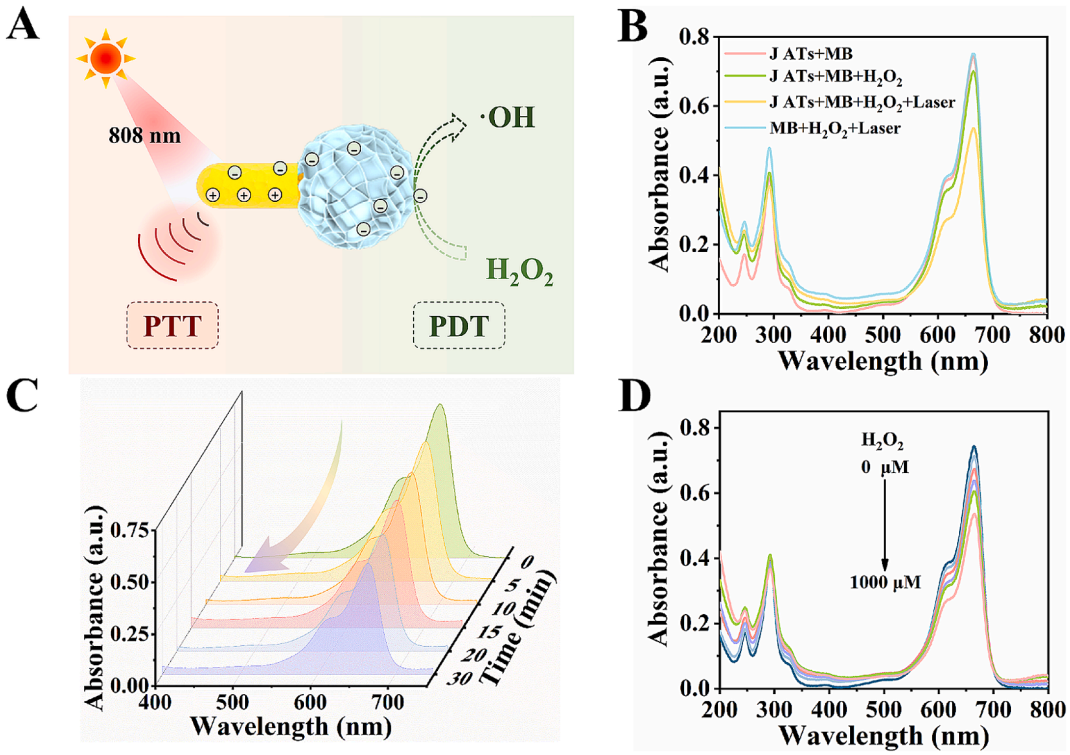

Fig. 2. (A) Schematic illustration showing PTT and PDT of J ATs under laser irradiation. (B) UV–Vis absorption spectra of MB under different conditions. (C) Variation of MB absorption intensity with different laser irradiation times. (D) UV–Vis spectra of MB at different H_2O_2 concentrations.

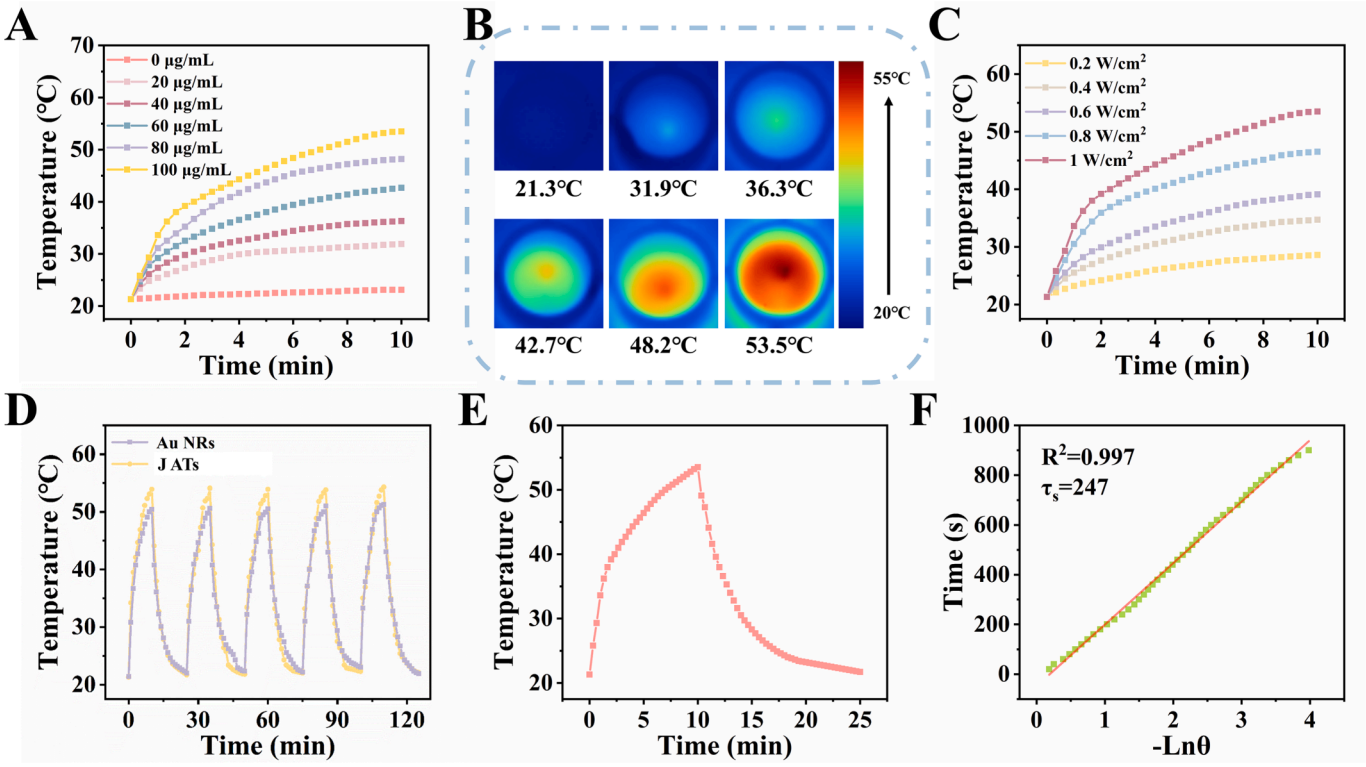

Fig. 3. (A) Time-dependent temperature curves of J ATs at different concentrations under 808 nm laser irradiation (1 W cm^{-2}) and (B) the corresponding thermographic images. (C) Temperature changes of the nanosensor (100 μg/mL) irradiated with a laser at different powers. (D) Laser On-Off temperature changes of Au NRs and J ATs. (E) Changes of temperature of J ATs during an On-Off cycle. (F) Negative logarithmic plot of time versus temperature driving force of (E).

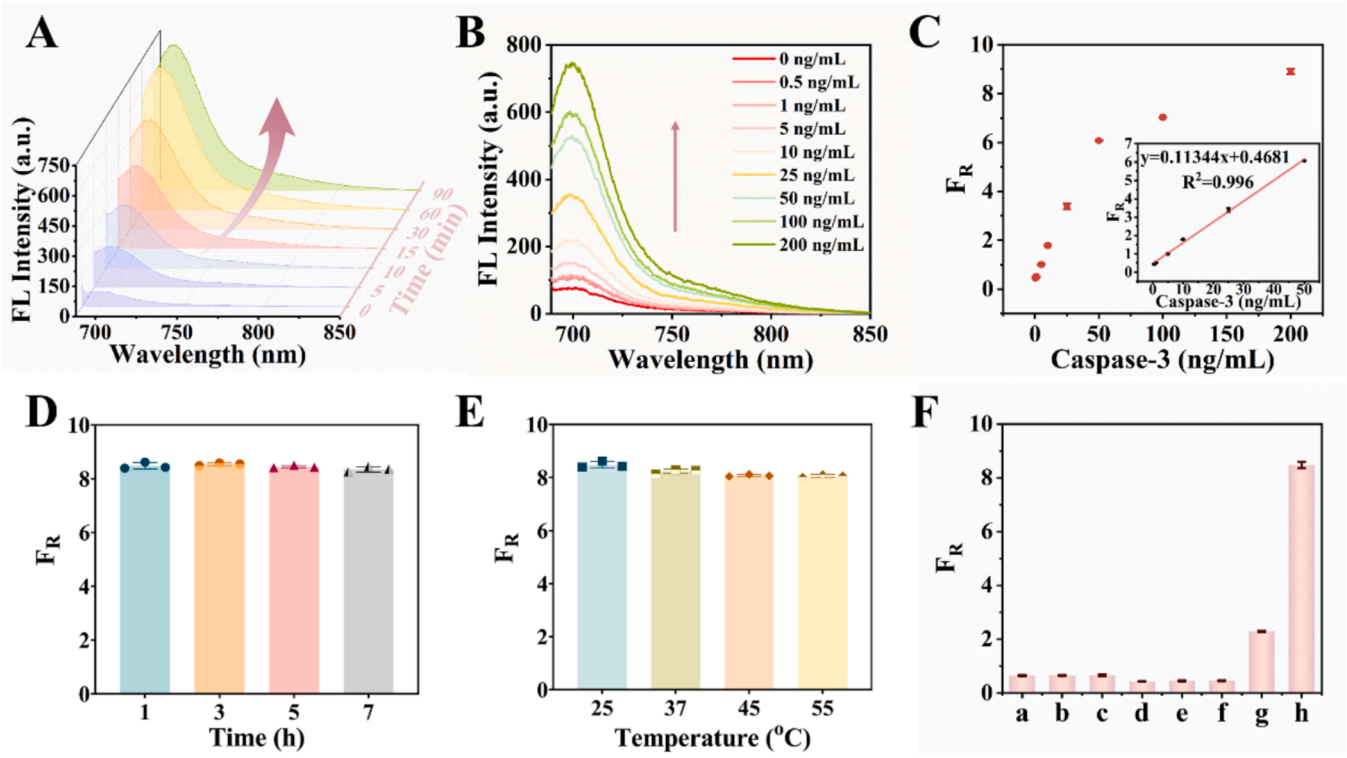

Fig. 4. (A) Fluorescence spectra of J ATPs incubated with 200 ng/mL caspase-3 for different time periods. (B) Fluorescence spectra of the enzyme at different concentrations incubated with the nanosensor for 60 min and (C) the corresponding F_R (F_R =(F-F_0)/F_0, F_0 is the fluorescence value of the blank sample) curve. The inset shows the linear correlation between enzyme concentration and fluorescence intensity. Responsiveness of the nanosensor to the enzyme after treatments at different times (D) and temperatures (E). (F) Selectivity of nanosensors towards various molecules (a: glutathione sulfurtransferase (GST); b: hyaluronidase; c: caspase-1; d: bovine serum albumin (BSA); e: glucose; f: carboxylesterase; g: caspase-3 + Z-DEVD-FMK; h: caspase-3).

used. Fig. 3A shows the mechanism of PTT and PDT of J ATs under laser irradiation. After laser irradiation for a certain period, the temperature of the nanoparticle increased significantly. Moreover, the increase in temperature was positively correlated with the concentration of nanoparticles. At a concentration of 100 μg/mL, the temperature reached 53.5 °C within 10 min, and the photothermal therapy had an impact on the tumor cells [48]. Under the same conditions, the temperature of water increased only up to 23.1 °C (Fig. 3B). At the same time, the increase in temperature was proportional to the laser power (Fig. 3C). Based on a previously reported study, we calculated the photothermal conversion efficiency (η) of the materials. The calculations, as has been shown in published reports, showed that η for Au NRs was 49.92 %, whereas that for J ATs was 55.41 % (Fig. 3D-3E and S12) [49]. To further assess the stability of the photothermal effect of the materials, the nanoparticle was subjected to repeated laser stimulation. We found that the ability of the materials could be well maintained in multiple "On-Off" cycles (Fig. 3F). On this basis, the photothermal capacity of J ATPZFs was also verified (Fig. S12A). It was found that the temperature of solution could rise to 52.5 °C under laser stimulation at the same time, which proved that J ATPZFs also had good photothermal capacity. Thus, the nanomaterials synthesized in this work were excellent photothermal imaging materials that could be used in the monitoring of therapeutic efficacy.

3.4. *In vitro sensing of caspase-3*

Nanosensors were designed to evaluate the therapy efficacy based on self-IIT. Thus, selecting a biomarker that is activated during the treatment process is key for achieving accurate detection. Caspase-3, an important enzyme activated during the apoptotic process, was selected as a detection marker and a prerequisite for the assessment of the therapy efficacy. We simulated this physiological process *in vitro* using J ATPs that remained after the breakdown of the MOF shell as a detection nanosensor and caspase-3, which was added to the system. The enzyme enabled the shearing of a specific site, resulting in the recovery of the fluorescent signal.

First, the nanosensors (100 μg/mL) were mixed with caspase-3, and the mixture was diluted with a buffer solution (the specific components can be found in supporting information) to caspase-3 concentration of 200 ng/mL. The mixture was placed in an incubator at a constant temperature of 37 °C, and the fluorescence signal was thereafter measured after different time periods. Finally, 60 min was selected as the optimal reaction time (Fig. 4A).

In subsequent experiments, the enzyme concentration in the reaction system was varied, and the relationship between fluorescence signal recovery and enzyme concentration was examined. The results showed that the fluorescence intensity (F_R=(F-F_0)/F_0) was positively correlated with the enzyme concentration (0–200 ng/mL). The correlation was linear in the enzyme concentration range of 0–50 ng/mL and the limit of detection (LOD) was 0.08 ng/mL (Fig. 4B and 4C).

Further experiments were conducted to assess the specificity of the nanosensor, in which other common biomarkers (proteins, enzymes, etc.) were chosen as interferences. The results (Fig. 4F) showed that there was no fluorescence signal enhancement. To further prove the data, the nanosensor was incubated with Z-DEVD-FMK (specific inhibitor of caspase-3) + caspase-3, from which the results showed a significant decrease in the signal. In addition, the stability of the nanosensor was subsequently verified (Fig. 4D and 4E). Overall, the data demonstrated that the nanosensor could detect caspase-3 in a limited manner, showing that it has the potential to be further applied in bio-imaging such as cellular applications, and as a tool for the evaluation of ionic interference therapies.

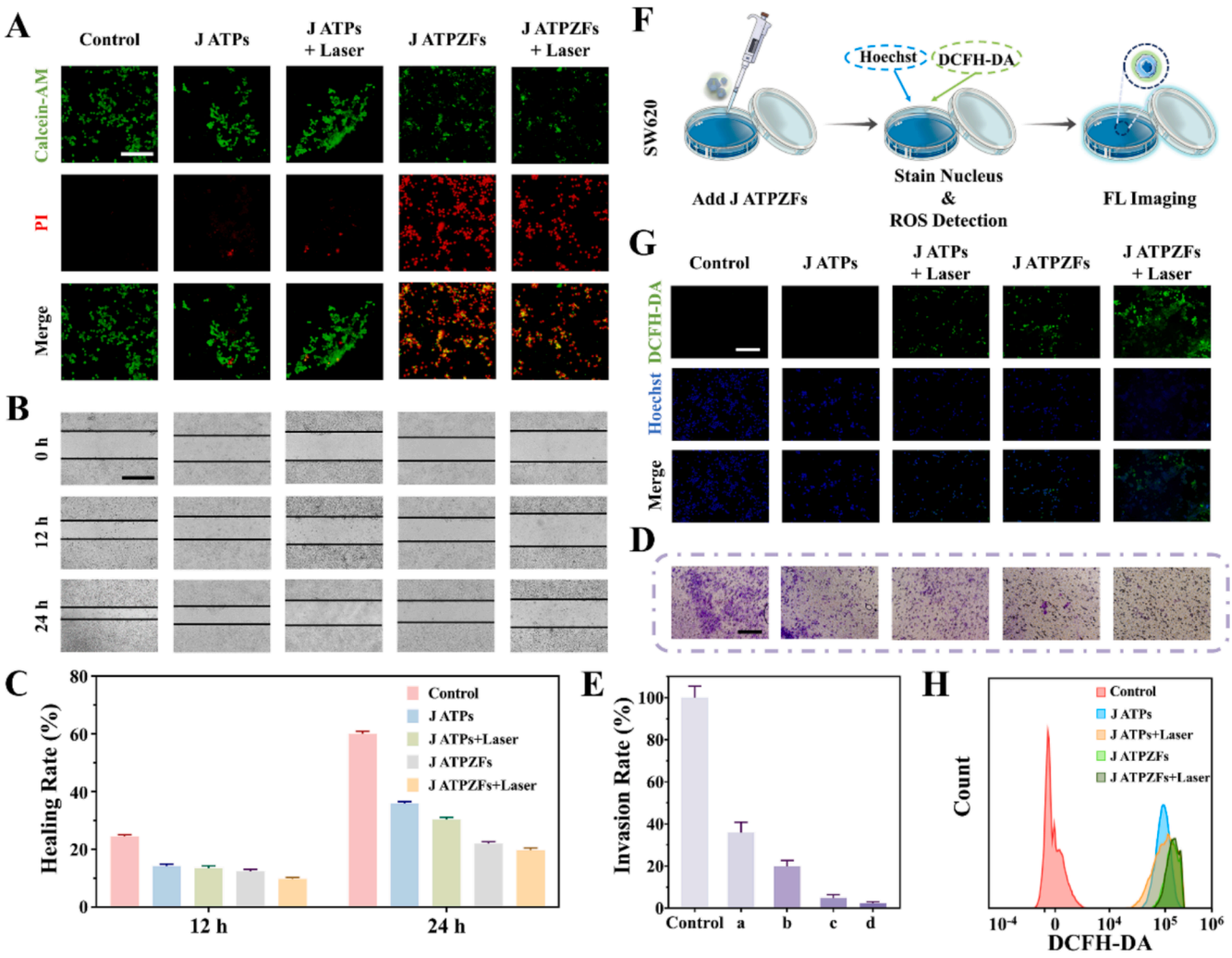

Fig. 5. (A) SW620 cells treated with different treatment conditions for 24 h. Calcein-AM (green, live cells) and PI (red, dead cells) (scale bar: 150 μm). (B) Cell migration assay under different conditions and (C) scratch wound healing rate of cells in each group (scale bar: 200 μm). (D) Illustration of Transwell invasion assay (scale bar: 150 μm) and (E) the corresponding invasion rate. (F) Staining assay of intracellular ROS. (G) Fluorescence images of SW620 cells stained with 4′,6-diaminidine-2-phenylindoline dihydrochloride (DAPI) and DCFH-DA after different treatments (scale bar: 150 μm) and (H) flow cytometry analysis.

3.5. Effects of nanosensors on tumor cells

Based on the successful development of the *in vitro* experiment, the feasibility of the nanosensors was verified. The cell experiments were then designed. It is necessary to evaluate the effects of the probe on cell viability before using it to visualize the efficacy. In this experiment, colon cancer cells (SW620) were selected.

The cells were incubated with the nanosensors at different concentrations, and the results are shown in Fig. S13. The addition of J ATPs had no significant effects on cell activity; by contrast, the addition of J ATPZFs markedly reduced cell viability, and the cell viability decreased with increasing incubation time. This result was in line with the above analysis. It is possible that the introduction of MOFs to J ATPZFs can cleave and generate a large amount of Zn^{2+} in response to the tumor microenvironment, which in turn triggers the IIT treatment and induces cell death [50,51].

To further demonstrate the effect of the nanosensors on cell viability, Calcein-AM and propidium iodide (PI) were used to stain the cells after incubation under different conditions. As shown in Fig. 5A, the cell viability of the J ATPs group and the blank control group were both unaffected. After being modified with ZIF-8, the nanosensor exhibited a significant effect on cell viability, and the fluorescence of the PI-stained part was enhanced, which was in line with the results from the above kits. After the addition of the nanosensors, the cells were irradiated with an additional 808 nm laser (1 W cm^{-2}, 10 min), and the results showed that the additional laser irradiation led to a further decrease in cell activity. In summary, the data demonstrate that the nanosensor has the IIT ability.

Studies have shown that cancer cells can migrate and invade, and additional drug treatment could inhibit these processes. To verify the effect of the nanosensor on the migration and invasion ability of tumor cells, "wound" and Transwell experiments were conducted. As shown in Fig. 5B and 5C, due to the high migration efficiency of tumor cells, the wound in the blank control group was healed after 24 h. The addition of the nanosensor and the irradiation with a laser inhibited the wound-healing process. This may be due to the nanosensor's ability to promote ROS production.

The results from the Transwell assay, in which cells were placed in the upper chamber and allowed to gradually invade the lower chamber, were similar to those from the wound-healing assay. In the control group, a large number of cells appeared due to the absence of external interference, but with the addition of nanoparticles, the invasion ability of cells was inhibited (Fig. 5D and 5E). These findings further confirm the above conclusions.

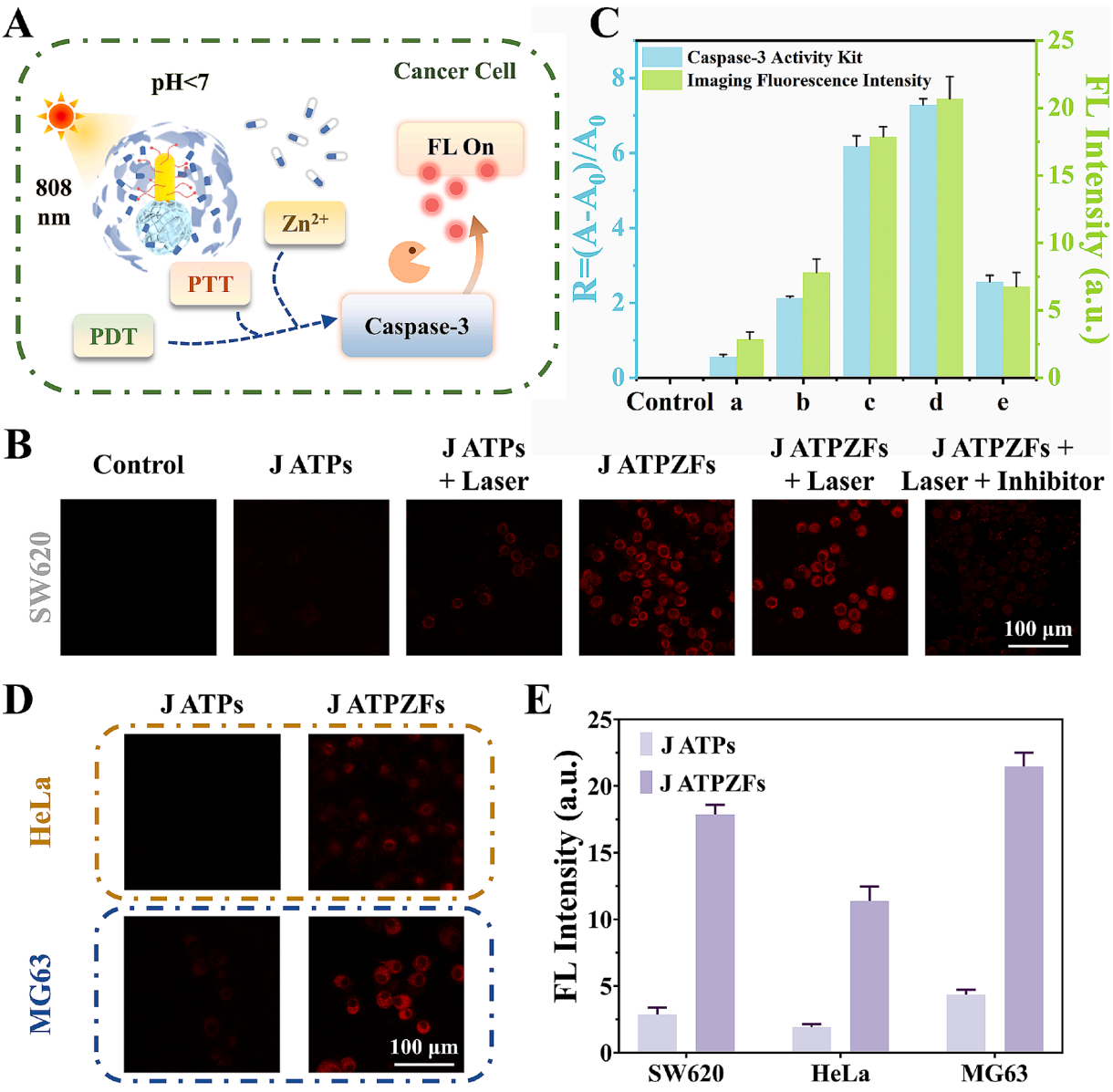

Fig. 6. (A) Schematic diagram illustrating the induction of intracellular caspase-3 activation by the nanosensor. (B) Fluorescence images of cells under different incubation conditions and (C) the corresponding fluorescence intensity and caspase-3 activity assay results (a: J ATPs, b: J ATPs + laser, c: J ATPZFs, d: J ATPZFs + laser, e: J ATPZFs + laser + inhibitor). (D) Fluorescence images of HeLa and MG63 co-cultured with the nanosensors and (E) the corresponding fluorescence intensity.

3.6. Ability of nanosensors to promote intracellular ROS production

The nanosensors were designed to promote ROS production upon laser stimulation by taking advantage of the special optical properties of TiO_2 with which they were modified. We first validated the ability of the nanosensor *in vitro*. To ensure that the nanosensor can be used in subsequent applications, its ·OH production ability was verified by cell experiments.

Herein, 2,7-dichlorodihydrofluorescent yellow diacetic acid (DCFH-DA) was selected as the fluorescent ROS detection probe. SW620 cells treated with different conditions were stained with DCFH-DA (Fig. 5F). The detection principle of DCFH-DA is as follows: after being hydrolyzed in cells, DCFH-DA can respond to ROS and be oxidized into fluorescent substances; and the strength of its fluorescence reflects the content of cellular ROS. The fluorescence images are shown in Fig. 5G. Untreated cells were used the blank control. To better locate the cells, their nuclei were stained with 4′,6-diaminidine 2-phenylindoline dihydrochloride (DAPI), which exhibits blue fluorescence, allowing the cell nuclei to be observed.

Whereas the control group did not exhibit the green fluorescence signal, the group incubated with the nanosensor containing TiO_2 and irradiated with an 808 nm laser appeared to promote the production of cellular ROS, as indicated by the increase in the fluorescence signal. The modification with ZIF-8 provides the nanosensor with the ability to respond to acidic environments and act as an exogenous donor for Zn^{2+}. The large enrichment of Zn^{2+} leads to mitochondrial ROS production, which can synergize the ability of TiO_2. The results showed that the addition of J ATPZFs or the irradiation with a laser could significantly enhance the fluorescence in the green channel, which is consistent with the above analysis. Meanwhile, flow cytometry was used to analyze the above conditions. The results shown in Fig. 5H are consistent with the conclusions of the previous analysis. This demonstrates that the nanosensor can be used as a visual tool for monitoring the efficacy of autologous-induced ion therapy.

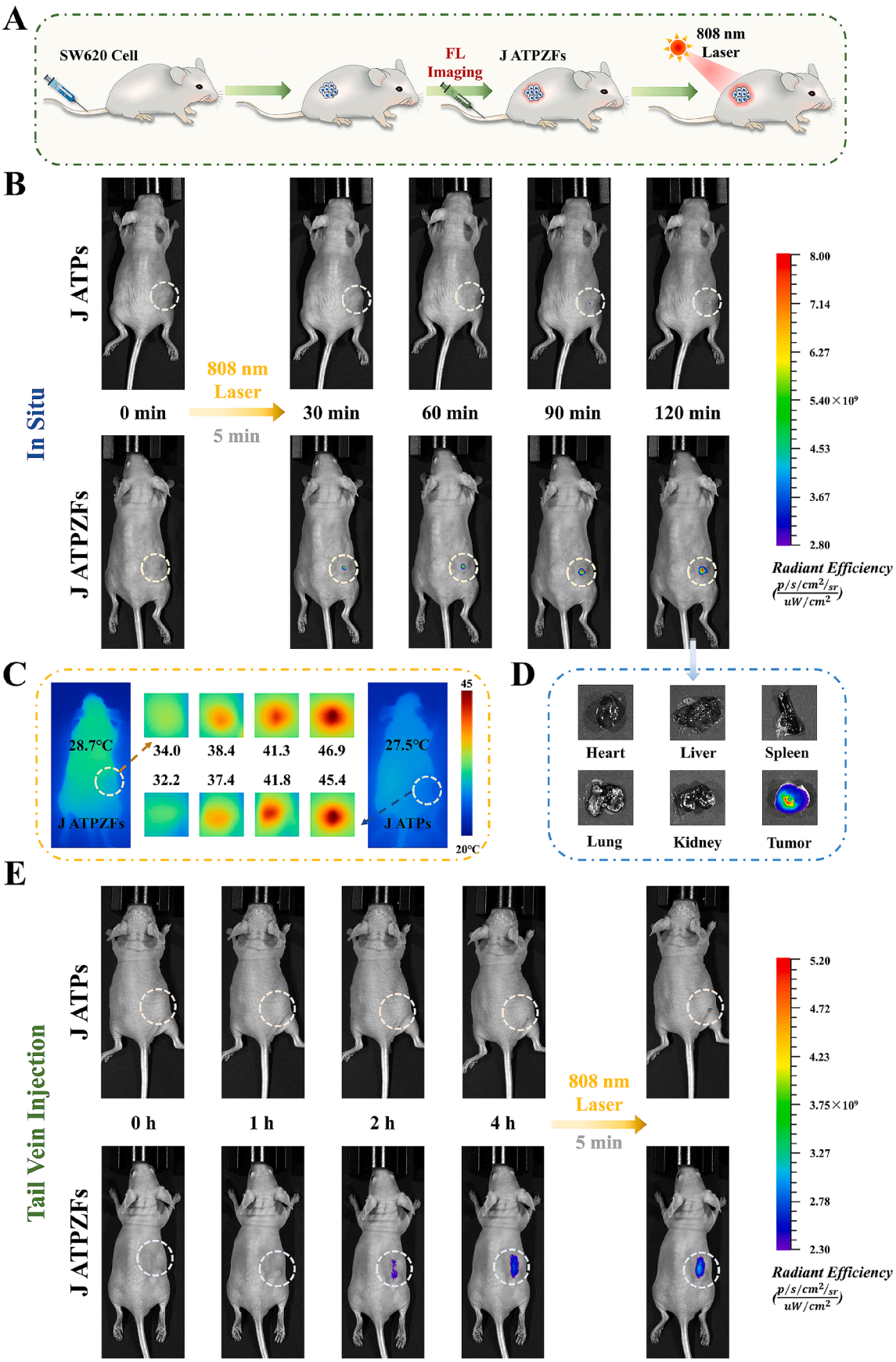

Fig. 7. (A) Schematic diagram showing the application of the nanosensors in *in vivo* imaging. (B) Fluorescence images of tumor-bearing mice after being injected with different nanosensors *in situ* and laser irradiation (1 W cm^{-2}). (C) Changes of temperature before and after laser irradiation of mice in (B). (D) Fluorescence images of mouse organs. (E) Images of the tumor site injected with the nanosensor through the tail vein.

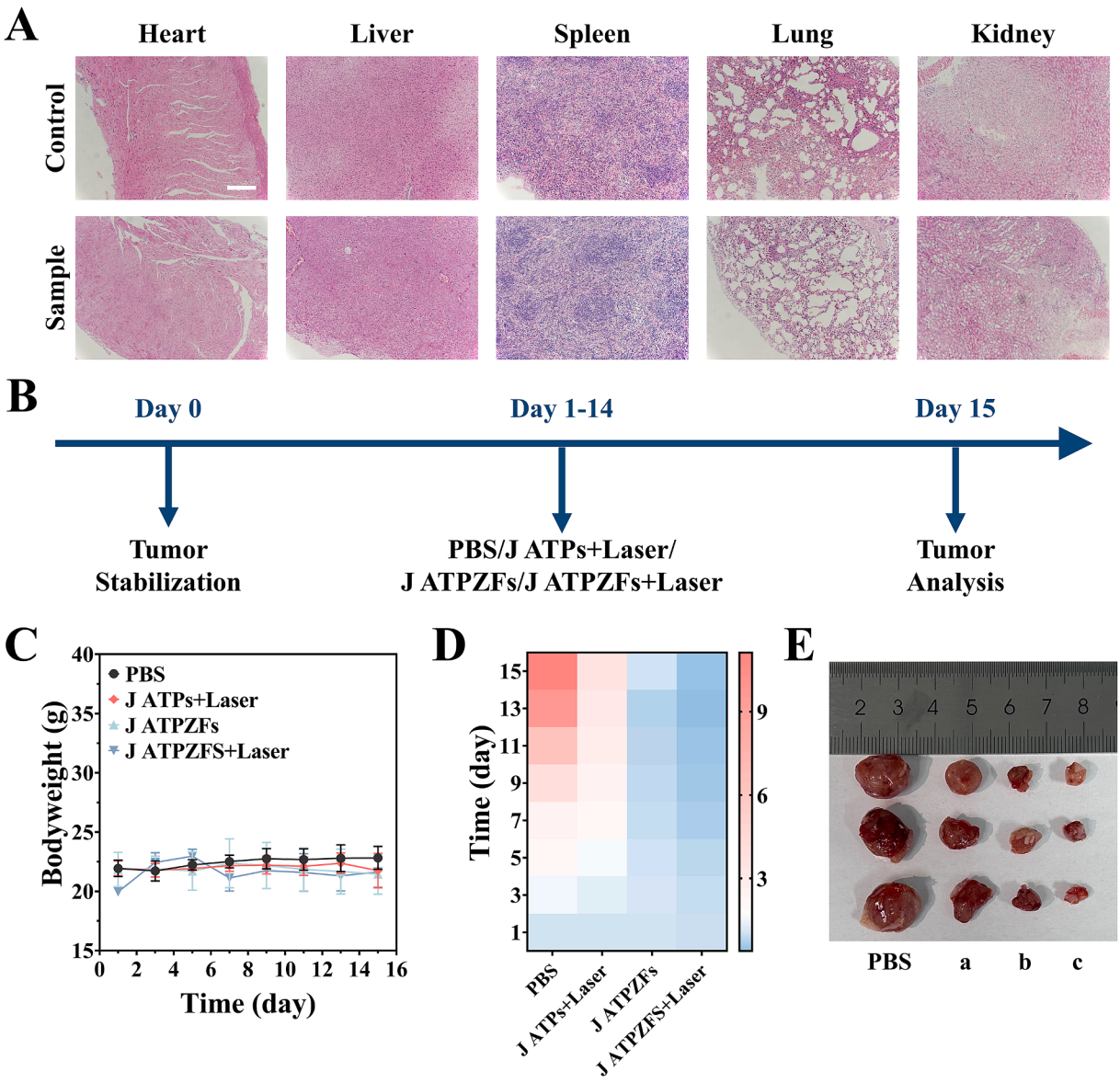

Fig. 8. (A) Histological analysis of mice after 30 days without injection (Control) and after injection (Sample) of nanosensors. The scale size is 200 μm. (B) Timeline for mouse treatment. (C) Body weight, (D) relative tumor volume (V/V_0) and (E) photographs of tumor of mice after different treatments (a: J ATPs + laser; b: J ATPZFs; c: J ATPZFs + laser).

3.7. In vitro imaging applications of J ATPZFs

Based on the above data, the nanosensor could auto-respond to TME, promote intracellular ROS production, and induce cell death. Additionally, without the modification of the MOFs structure, the cell activity was not affected. The nanosensor was further applied in the imaging of intracellular IIT using colon cancer cell SW620 as the cell model. The reaction mechanism is shown in Fig. 6A. Firstly, the appropriate incubation time was selected based on the time optimization experiment. Considering cell morphology and effects on imaging, 24 h was selected (Fig. S14).

Firstly, the images of cells under different conditions, which can infer the cell state according to the strength of the fluorescence signal, were compared. The influence of IIT on the cells was then assessed. As shown in Fig. 6B and 6C, fluorescence signals were not observed after the introduction of J ATPs alone, which is indicative of the nontoxicity of the nanosensors. On this basis, the fluorescence signals appeared after laser irradiation, likely due to the promotion of ROS production by TiO_2, which induces apoptosis. By contrast, the modification of J ATPZFs by ZIF-8 resulted in the increase in Zn^{2+} in TME, which also led to the increase in ROS content, in turn causing the activation of caspase-3 in the apoptosis pathway and the enhancement of the fluorescence signal. Under this condition, the subsequent irradiation with a laser led to further enhancement, which then synergistically enhanced the ROS generation and the fluorescence signal. The addition of inhibitors led to the reduction of fluorescence, further confirming that the recovery of fluorescence signal was due to the cleavage of the peptide chain by the enzyme. In addition, cells treated under different conditions were lysed and tested with caspase-3 activity kit. Fig. 6C showed that the activity of intracellular caspase-3 was basically consistent with the trend of fluorescence intensity, which also proved the ability of J ATPZFs to visually feedback intracellular enzyme activity.

Because caspase-3 can be turned on during apoptosis, the nanosensor could be applied to evaluate the efficacy of various diseases. To prove this approach, the nanosensor was incubated with HeLa and MG63 cells. As shown in Fig. 6D and 6E, the nanosensor could provide visual feedback on the efficacy in different cell types, which confirms its suitability in this application. The successful development of this experiment, in

which the nanosensors were proven to have the ability to evaluate the efficacy of the therapy method, laid a good foundation for subsequent *in vivo* experiments.

3.8. In vivo imaging applications of J ATPZFs

To facilitate the irradiation of 808 nm laser, SW620 tumor-bearing mice were generated and used for *in vivo* imaging experiments (Fig. 7A). The *in vivo* toxicity of the nanosensors was evaluated prior to *in vivo* experiments. Fig. 8A showed that the organs of mice did not show significant damage after injection of the nanosensors, and there was no difference in blood routine analysis before and after injection (Table S1). And the low biotoxicity of J ATPs was confirmed by hemolysis experiments before conducting the subsequent *in vivo* imaging experiments (Fig. S15).

To assess their capability in visual monitoring of therapeutic effects, J ATPs and J ATPZFs nanosensors were directly injected at the tumor site. The results (Figs. 7B, 7C and S16) illustrated that following laser irradiation (1 W cm^{-2}, 5 min), the J ATPs group exhibited weak fluorescence, whereas the J ATPZFs group exhibited distinct fluorescence. During laser irradiation, the changes in temperatures at the tumor sites were recorded, and the data showed that the temperatures increased to 46.9 °C and 45.4 °C, respectively (Fig. 7D). This is consistent with previous findings, which confirm that the nanosensor can function as a Zn^{2+} donor to activate caspase-3 and enhance PDT and PTT effects, in turn leading to fluorescence recovery.

Furthermore, we incorporated FA, a tumor-targeting agent, into the nanosensor via self-assembly. To verify the nanosensor's enrichment at the tumor site, we injected tumor-bearing mice with the probe through tail vein and then performed imaging at various time points. As shown in Fig. 7E and S16, the fluorescence signal at the tumor site in the J ATPZFs group was intensified significantly after 4 h, but there was no obvious fluorescence signal in the J ATPs group, which confirms the accumulation of the nanosensor. Additionally, subsequent laser irradiation at the tumor site led to further fluorescence enhancement, which demonstrated the responsiveness of the probe to the laser irradiation.

Given the promising outcomes of the *in vivo* imaging and *in vitro* studies, further *in vivo* experiments were carried out to evaluate the therapeutic efficacy of the nanosensor-assisted treatment (Fig. 8B). Tumor growth inhibition across various treatment groups was assessed: PBS, J ATPs + laser (Group a), J ATPZFs (Group b), and J ATPZFs + laser (Group c). The body weight and tumor size were recorded every other day during treatment. The results (Fig. 8C) showed that the body weight was stable throughout the experimental period, indicating that the nanosensor has low toxicity. The tumor volume data (Fig. 8D and 8E) revealed a notable anticancer effect, with the J ATPZFs + 808 nm laser group achieving the most significant tumor volume reduction (V/V_0 = 0.46). All treatment groups (a, b, c) demonstrated significant tumor growth inhibition compared to the PBS group. Group a represented the PDT and PTT therapeutic effects under laser irradiation, while groups b and c demonstrated the IIT and synergistic therapeutic efficacy, respectively. These findings align with the *in vitro* data, confirming that the nanosensor has potential in adjuvant therapies.

Overall, the developed nanosensors could successfully facilitate both *in vivo* and *in vitro* imaging and real-time monitoring of efficacy through self-induced IIT. The nanosensors also have a certain universality and can realize the evaluation of efficacy in other diseases, which shows that they have good application prospects.

4. Conclusion

In summary, J ATPZFs, a self-induced IIT nanosensor capable of simultaneous imaging, was successfully designed and synthesized, and employed for visual evaluation of the efficacy of cancer therapy and adjuvant therapy. After J ATPZFs entered the cell, the ZIF-8 structure of their outer layer was broken and simultaneously, a large amount of Zn^{2+} was released, resulting in the abnormal accumulation of Zn^{2+} in cells and the promotion of ROS production. On this basis, assisted by 808 nm laser irradiation, PDT and PTT played an auxiliary role in activating the caspase-3 to cleave the peptide chain in the apoptotic pathway, and as a result, the fluorescence signal could be restored. Based on the above principle, the nanosensor was successfully applied in *in vitro* and *in vivo* imaging and therapy. According to the imaging results, additional localized laser irradiation could be used to promote adjuvant treatment, which has an excellent guiding effect. This work provides a basis for the future clinical development of visual prognosis assessment strategies.

CRediT authorship contribution statement

Jukun Yang: Writing – original draft, Investigation, Formal analysis, Data curation, Conceptualization. **Mo Ma:** Investigation, Data curation. **Chen Zhao:** Investigation, Data curation. **Yuxuan Chen:** Investigation, Formal analysis. **Jingdan Sun:** Investigation. **Ying Sun:** Project administration, Data curation. **Pinyi Ma:** Writing – review & editing, Project administration, Data curation, Conceptualization. **Shan Jiao:** Project administration, Data curation. **Daqian Song:** Supervision, Resources, Project administration, Funding acquisition.

Declaration of competing interest

The authors declare that they have no known competing financial interests or personal relationships that could have appeared to influence the work reported in this paper.

Acknowledgments

This work was supported by the National Key R&D Program of China (2021YFF0600701), the National Natural Science Foundation of China (22074052 and 22004046) and the Science and Technology Developing Foundation of Jilin Province of China (20230101033JC).

Appendix A. Supplementary data

Supplementary data to this article can be found online at https://doi.org/10.1016/j.cej.2025.161091. Materials, instruments, synthesis of Au NRs, photothermal performance verification, cell counting kit-8 (CCK-8) assay, Calcein AM/Propidium Iodide (PI) staining, *in vitro* migration assay, transwell invasion assay, hemolysis assay, establishment of tumor model supplementary figures.

Data availability

Data will be made available on request.

References

[1] C. Willyard, The Colon Cancer Conundrum, Nature (2021), https://doi.org/10.1038/d41586-021-03405-6.
[2] A. Hijazi, J. Galon, Principles of Risk Assessment in Colon Cancer: immunity is key, OncoImmunology 13 (1) (2024) 2347441.
[3] A. Gunjur, Short vs Long Course Adjuvant Chemotherapy for Colon Cancer, Lancet Oncol. 19 (5) (2018) e236.
[4] S.-N. Jia, Y.-B. Han, R. Yang, Z.-C. Yang, Chemokines in Colon Cancer Progression, Semin. Cancer Bio. 86 (2022) 400–407.
[5] A. Audisio, R. Fazio, V. Daprà, I. Assaf, A. Hendlisz, F. Sclafani, Neoadjuvant Chemotherapy for Early-Stage Colon Cancer, Cancer Treat. Rev. 123 (2024) 102676.
[6] P.R. Galle, F. Tovoli, F. Foerster, M.A. Wörns, A. Cucchetti, L. Bolondi, The Treatment of Intermediate Stage Tumours Beyond TACE: From Surgery to Systemic Therapy, J. Hepatol. 67 (1) (2017) 173–183.
[7] O.U. Akakuru, Z. Zhang, M.Z. Iqbal, C. Zhu, Y. Zhang, A. Wu, Chemotherapeutic Nanomaterials in Tumor Boundary Delineation: Prospects for Effective Tumor Treatment, Acta Pharm. Sin. B 12 (6) (2022) 2640–2657.
[8] L. Zhang, X. Du, Q. Li, L. Qian, J. Chen, C. Liu, Q. Yu, Z. Gan, A Multimodal Therapeutic Nanoplatform Overcoming Tumor Hypoxia Heterogeneity for Improved Tumor Chemoradiotherapy, Adv. Funct. Mater. 32 (34) (2022) 2204629.

[9] H. Luo, W. Ma, Q. Chen, Z. Yang, Y. Dai, Radiotherapy-Activated Tumor Immune Microenvironment: Realizing Radiotherapy-Immunity Combination Therapy Strategies, Nano Today 53 (2023) 102042.

[10] H. Dou, Z. Luo, H. Wang, Q. Duan, Z. Jiang, H. Chen, N. Tan, Tumor Microenvironment-Responsive Intelligent Nanoplatform with Oxygen Self-Supply for Synergistic Chemotherapy/Photodynamic Therapy/Photothermal Therapy Against Hypoxic Tumors, Chem. Eng. J. 487 (2024) 150523.

[11] J. Liu, F. Wu, M. Wang, M. Tao, Z. Liu, Z. Hai, Caspase-3-Responsive Fluorescent/Photoacoustic Imaging of Tumor Apoptosis, Anal. Chem. 95 (25) (2023) 9404–9408.

[12] L. Teng, X. Han, Y. Liu, C. Lu, B. Yin, S. Huan, X. Yin, X.B. Zhang, G. Song, Smart Nanozyme Platform with Activity-Correlated Ratiometric Molecular Imaging for Predicting Therapeutic Effects, Angew. Chem. Int. Ed. 60 (50) (2021) 26142–26150.

[13] Z. Zhang, R. Wang, R. Luo, J. Zhu, X. Huang, W. Liu, F. Liu, F. Feng, W. Qu, An Activatable Theranostic Nanoprobe for Dual-Modal Imaging-Guided Photodynamic Therapy with Self-Reporting of Sensitizer Activation and Therapeutic Effect, ACS Nano 15 (3) (2021) 5366–5383.

[14] Q. Wu, K.Y. Zhang, P. Dai, H. Zhu, Y. Wang, L. Song, L. Wang, S. Liu, Q. Zhao, W. Huang, Bioorthogonal "Labeling after Recognition" Affording an FRET-Based Luminescent Probe for Detecting and Imaging Caspase-3 via Photoluminescence Lifetime Imaging, J. Am. Chem. Soc. 142 (2) (2019) 1057–1064.

[15] D.M. Charron, G. Zheng, Nanomedicine development guided by FRET imaging, Nano Today 18 (2018) 124–136.

[16] K. Xu, M. Guo, X. Sun, X. Xie, Y. Cai, X. Dong, J. Shao, FRET-Engineering of Organic Nanoparticles for Photoacoustic Imaging-Guided Photodynamic and Augmented Photothermal Therapy, Sens. Actuators B Chem. 401 (2024) 135091.

[17] J.T. Burgess, E. Bolderson, M.N. Adams, A.-M. Baird, S.-D. Zhang, K.A. Gately, K. Umezawa, K.J. O'Byrne, D.J. Richard, Activation and cleavage of SASH1 by caspase-3 mediates an apoptotic response, Cell Death Dis. 7 (11) (2016) e2469–e.

[18] N.B. Hentzen, R. Mogaki, S. Otake, K. Okuro, T. Aida, Intracellular Photoactivation of Caspase-3 by Molecular Glues for Spatiotemporal Apoptosis Induction, J. Am. Chem. Soc. 142 (18) (2020) 8080–8084.

[19] B. Esteban-Fernández de Ávila, D.E. Ramírez-Herrera, S. Campuzano, P. Angsantikul, L. Zhang, J. Wang, Nanomotor-Enabled pH-Responsive Intracellular Delivery of Caspase-3: Toward Rapid Cell Apoptosis, ACS Nano 11 (6) (2017) 5367–5374.

[20] W. Zhu, C.-Y. Wang, J.-M. Hu, A.-G. Shen, Promoted "Click" SERS Detection for Precise Intracellular Imaging of Caspase-3, Anal. Chem. 93 (11) (2021) 4876–4883.

[21] M. Wang, W. Liu, B. Li, W. Zhu, D. Li, J. Li, Z. Hai, An Integrative Probe for Tumor Therapy and Dual-Modal Self-Evaluation Imaging of Therapeutic Efficacy, ACS Mate. Lett. 6 (10) (2024) 4617–4623.

[22] H.-D. Xu, X. Cheng, X. Sun, P. Chen, W. Zhan, X. Liu, X. Wang, B. Hu, G. Liang, Caspase-3-Triggered Intracellular Gadolinium Nanoparticle Formation for T1-Weighted Magnetic Resonance Imaging of Apoptosis In Vivo, Nano Lett. 23 (13) (2023) 6178–6183.

[23] Y. Cao, S. Li, C. Chen, D. Wang, T. Wu, H. Dong, X. Zhang, Rattle-Type Au@$Cu_{2-x}S$ Hollow Mesoporous Nanocrystals with Enhanced Photothermal Efficiency for Intracellular Oncogenic MicroRNA Detection and Chemo-Photothermal Therapy, Biomaterials 158 (2018) 23–33.

[24] X. Kong, X. He, F. He, Y. Li, Y. Feng, Y. Li, Z. Luo, J.-W. Shen, Y. Duan, Sandwich Layer-Modified Ω-Shaped Fiber-Optic LSPR Enables the Development of an Aptasensor for a Cytosensing–Photothermal Therapy Circuit, ACS Sens. 9 (9) (2024) 4637–4645.

[25] X. Yu, K. Yang, X. Chen, W. Li, Black Hollow Silicon Oxide Nanoparticles as Highly Efficient Photothermal Agents in the Second Near-Infrared Window for In Vivo Cancer Therapy, Biomaterials 143 (2017) 120–129.

[26] Z. Hu, X. Zhou, W. Zhang, L. Zhang, L. Li, Y. Gao, C. Wang, Photothermal Amplified Multizyme Activity for Synergistic Photothermal-Catalytic Tumor Therapy, J. Colloid Interf. Sci. 679 (2025) 375–383.

[27] Y.Z. Liu, X.Y. Ran, D.H. Zhou, H. Zhang, Y.J. Chen, J.X. Xu, S.Y. Chen, Q.Q. Kong, X.Q. Yu, K. Li, Novel Dibenzofulvene-Based NIR-II Emission Phototheranostic Agent with an 82.6% Photothermal Conversion Efficiency for Photothermal Therapy, Adv. Funct. Mater. 34 (8) (2023) 2311365.

[28] Y. Yu, H. Wang, Z. Zhuang, C. Ji, L. Zhang, Y. Li, Z. Zhao, D. Ding, G. Feng, B. Z. Tang, Self-Adaptive Photodynamic-to-Photothermal Switch for Smart Antitumor Photoimmunotherapy, ACS Nano 18 (20) (2024) 13019–13034.

[29] Z. Wang, M. Wang, X. Wang, Z. Hao, S. Han, T. Wang, H. Zhang, Photothermal-Based Nanomaterials and Photothermal-Sensing: An Overview, Biosens. Bioelectron. 220 (2023) 114883.

[30] S. Qu, Y. Ji, L. Fan, T. Yan, G. Zhu, H. Song, K. Yang, X. Han, Light-Enhanced Hypoxia-Responsive Gene Editing for Hypoxia-Resistant Photodynamic and Immunotherapy, Adv. Healthc. Mater. 13 (7) (2023) 2302615.

[31] S. Xiao, Y. Lu, M. Feng, M. Dong, Z. Cao, X. Zhang, Y. Chen, J. Liu, Multifunctional FeS_2 Theranostic Nanoparticles for Photothermal-Enhanced Chemodynamic/Photodynamic Cancer Therapy and Photoacoustic Imaging, Chem. Eng. J. 396 (2020) 125294.

[32] H. Wang, J. Chang, M. Shi, W. Pan, N. Li, B. Tang, A Dual-Targeted Organic Photothermal Agent for Enhanced Photothermal Therapy, Angew. Chem. Int. Ed. 58 (4) (2018) 1057–1061.

[33] M. Uusitalo, M. Strach, G. Eriksson, T. Dmytrenko, J. Andersson, A. Dahlin, M. Hulander, M. Andersson, Photothermal Properties of Solid-Supported Gold Nanorods, Nano Lett. 24 (40) (2024) 12529–12535.

[34] D. Aguilar-Ferrer, T. Vasileiadis, I. Iatsunskyi, M. Ziółek, K. Żebrowska, O. Ivashchenko, P. Błaszkiewicz, B. Grześkowiak, R. Pazos, S. Moya, M. Bechelany, E. Coy, Understanding the Photothermal and Photocatalytic Mechanism of Polydopamine Coated Gold Nanorods, Adv. Funct. Mater. 33 (43) (2023) 2304208.

[35] X. Guan, B. Wang, Y. Zhang, G. Qi, L. Chen, Y. Jin, Monitoring Stress Response Difference in Nucleolus Morphology and ATP Content Changes during Hyperthermia Cell Apoptosis with Plasmonic Fluorescent Nanoprobes, Anal. Chem. 94 (40) (2022) 13842–13851.

[36] F. Zhao, L. Liang, H. Wang, C. Wang, D. Su, Y. Ying, W. Li, J. Li, J. Zheng, L. Qiao, X. Mou, S. Che, J. Yu, H_2S-Activated Ion-Interference Therapy: A Novel Tumor Targeted Therapy Based on Copper-Overload-Mediated Cuproptosis and Pyroptosis, Adv. Funct. Mater. 33 (38) (2023) 2300941.

[37] S. Li, R. Fan, Y. Wang, K. He, J. Xu, H. Li, Application of Calcium Overload-Based Ion Interference Therapy in Tumor Treatment: Strategies, Outcomes, and Prospects, Front. Pharmacol. 15 (2024) 13523377.

[38] F. Fu, W. Wang, L. Wu, W. Wang, Z. Huang, Y. Huang, C. Wu, X. Pan, Inhalable Biomineralized Liposomes for Cyclic Ca^{2+}-Burst-Centered Endoplasmic Reticulum Stress Enhanced Lung Cancer Ferroptosis Therapy, ACS Nano 17 (6) (2023) 5486–5502.

[39] Y. Wei, J. Wang, S. Wu, R. Zhou, K. Zhang, Z. Zhang, J. Liu, S. Qin, J. Shi, Nanomaterial-Based Zinc Ion Interference Therapy to Combat Bacterial Infections, Front. Immunol. 13 (2022) 899992.

[40] L.-S. Lin, J.-F. Wang, J. Song, Y. Liu, G. Zhu, Y. Dai, Z. Shen, R. Tian, J. Song, Z. Wang, W. Tang, G. Yu, Z. Zhou, Z. Yang, T. Huang, G. Niu, H.-H. Yang, Z.-Y. Chen, X. Chen, Cooperation of Endogenous and Exogenous Reactive Oxygen Species Induced by Zinc Peroxide Nanoparticles to Enhance Oxidative Stress-Based Cancer Therapy, Theranostics 9 (24) (2019) 7200–7209.

[41] W. Jia, B. Jin, W. Xu, S. Liu, X. Mao, H. Peng, Y. Zhang, pH-Responsive and Actively Targeted Metal–Organic Framework Structures for Multimodal Antitumor Therapy and Inhibition of Tumor Invasion and Metastasis, ACS Appl. Mater. Interfaces 15 (43) (2023) 50069–50082.

[42] M. Yu, G. Zhang, P. Li, H. Lu, W. Tang, X. Yang, R. Huang, F. Yu, W. Wu, Y. Xiao, X. Xing, Acid-Activated ROS Generator with Folic Acid Targeting for Bacterial Biofilm Elimination, Mater. Sci. Eng. C-Mater 127 (2021) 112225.

[43] L. Popp, V. Tran, R. Patel, L. Segatori, Autophagic Response to Cellular Exposure to Titanium Dioxide Nanoparticles, Acta Bio. 79 (2018) 354–363.

[44] B. Wu, D. Liu, S. Mubeen, T.T. Chuong, M. Moskovits, G.D. Stucky, Anisotropic Growth of TiO2 onto Gold Nanorods for Plasmon-Enhanced Hydrogen Production from Water Reduction, J. Am. Chem. Soc. 138 (4) (2016) 1114–1117.

[45] M. Wang, X. Zhang, Q. Chang, H. Zhang, Z. Zhang, K. Li, H. Liu, D. Liu, L. An, Q. Tian, Tumor Microenvironment–Mediated NIR-I-to-NIR-II Transformation of Au Self-Assembly for Theranostics, Acta Bio. 168 (2023) 606–616.

[46] Y. Chen, H. Xiang, S. Zhuang, Y. Shen, Y. Chen, J. Zhang, Oxygen-Independent Photocleavage of Radical Nanogenerator for Near-IR-Gated and H_2O-Mediated Free-Radical Nanotherapy, Adv. Mater. 33 (36) (2021).

[47] W. Dai, R. Shu, F. Yang, B. Li, H.M. Johnson, S. Yu, H. Yang, Y.K. Chan, W. Yang, D. Bai, Y. Deng, Engineered Bio-Heterojunction Confers Extra- and Intracellular Bacterial Ferroptosis and Hunger-Triggered Cell Protection for Diabetic Wound Repair, Adv. Mater. 36 (9) (2024) 2305277.

[48] Q. Zhang, J. Wu, J. Wang, X. Wang, C. Wu, M. Chen, Q. Wu, M.S. Lesniak, Y. Mi, Y. Cheng, Q. Wang, A Neutrophil-Inspired Supramolecular Nanogel for Magnetocaloric–Enzymatic Tandem Therapy, Angew. Chem. Int. Ed. 59 (9) (2020) 3732–3738.

[49] L. Liu, X. Li, H. Zhang, H. Chen, M.M.A. Abualrejal, D. Song, Z. Wang, Six-in-One Peptide Functionalized Upconversion@Polydopamine Nanoparticle-Based Ratiometric Fluorescence Sensing Platform for Real-Time Evaluating Anticancer Efficacy Through Monitoring Caspase-3 Activity, Sens. Actuators B Chem. 333 (2021) 129554.

[50] S. Zhi, J. Zheng, Y. Yan, Y. Wang, C. Wu, S. Bi, Enzymatic Interlocking Aptamer-Micelles for Enhanced Cellular Internalization and Nucleus-Targeted Cancer Phototherapy, J. Colloid Interf. Sci. 678 (2025) 1132–1141.

[51] S. Zhi, X. Zhang, J. Zhang, X.-Y. Wang, S. Bi, Functional Nucleic Acids-Engineered Bio-Barcode Nanoplatforms for Targeted Synergistic Therapy of Multidrug-Resistant Cancer, ACS Nano 17 (14) (2023) 13533–13544.